Supplementary Materials for

Dual-State Stepwise Methane-to-Methanol Conversion by Water Droplets with Excellent Yield and Selectivity

Songtao Tang[1, 5 *], Kejian Li[1, 5], Jan Paul Menzel[2, 3, 5], Zhengwei Ye[1], Zhuoran Long[2, 3], Kai Sun[4], Victor S. Batista[2, 3*], Zetian Mi[1 *]

This PDF file includes:

Materials and Methods: S1-S12

Figures: S1 to S22

Tables: S1-S4

References

Materials and Methods

S1. Materials Preparation

The Ag-loaded photocatalysts (Ag/ZnO, Ag/CeO_2, Ag/TiO_2, and Ag/g-C_3N_4) were prepared by a photodeposition method. In a typical run, 30 μL of $AgNO_3$ solution (0.20 M) was added to 16 mL of deionized water, followed by 4 mL of methanol as a sacrificial electron donor. Subsequently, 0.30 g of commercial ZnO (99.9%, Sigma-Aldrich), TiO_2 (anatase, 99.5%, Sigma 718467), CeO_2 (99.9%, Sigma-Aldrich 544841), or g-C_3N_4 (99%, ACS Materials) was introduced, and the resulting suspension was transferred to a glass chamber for photodeposition. The chamber will then be evacuated using a vacuum pump for two minutes and irradiated under a xenon lamp for 30 minutes. After photodeposition, the solids were subjected to multiple washes with deionized water and centrifugation to remove residual solution, and then dried overnight in a vacuum oven at 60 °C. The preparation process of low-crystalline zinc oxide catalyst loading silver is presented following. Ammonia-water solutions with mass concentrations of 10% and 2% are prepared, and excess zinc hydroxide is added to the ammonia-water solution. In alkaline solution, zinc hydroxide can dissolve to generate hydroxozincate. When zinc hydroxide is excess, the concentration of hydroxozincate depends on the concentration of ammonia. After standing overnight, the upper transparent liquid is collected and stored in the refrigerator at a low temperature. Then, 0.3 g of ZnO/Ag powder were added into 3 mL of ammonium hydroxozincate solution. After mixing thoroughly, the excess liquid is quickly filtered off, and the powder with hydroxozincate ions on the surface is placed in a vacuum oven at 90 °C overnight for drying. The ammonia remaining on the surface of the zinc oxide powder evaporates. After dehydration of the hydroxozincate ions, a low-crystalline zinc oxide layer is formed on the surface of the crystalline zinc oxide particles. The dried powder is subjected to the same photodeposition method to deposit silver metal again. We synthesized low-crystalline/high-crystalline core-shell zinc oxide samples using ammonium hydroxozincate solutions with mass concentrations of 2% and 10%, labeled as LC-ZnO/Ag-1 and LC-ZnO/Ag-2, respectively.

S2. Methane Oxidation Experiments

The aqueous-phase methane oxidation is carried out in a 150 mL stainless steel reactor with

PTFE inner layer with a quartz window for light irradiation under different pressures. A 300 W Xe lamp (full spectrum light, 15 suns) is used as the light source. Typically, 100 mg catalyst is first dispersed in 20 mL of deionized water, and the mixture is added to the reactor cell. Then, the reactor is sealed and purged with argon for 1.5 h to remove the air and then purged with methane for 30 mins to replace the Ar. The reaction time is 2 hours.

The conventional stepwise methane oxidation is conducted in a 30 mL glass reactor. A 300 W Xe lamp (full spectrum light, 15 suns) is used as the light source. The catalyst (~200 mg) is supported on a ceramic wool bed (SiO_2: 50%, Al_2O_3: 50%), which is placed in the center of the glass reactor. Prior to each methane oxidation cycle, the glass reactor and the catalyst bed are dried in a vacuum oven at 90 °C for 12 hours to remove any residual moisture. Argon gas is then purged for 2 hours to eliminate any remaining oxygen in the reactor, creating an oxygen-free environment. Subsequently, CH_4/Ar (1:3) gas with a flow rate of 20 sccm is purged for 30 minutes to replace the argon gas in the reactor. During the reaction, the CH_4/Ar flow rate is maintained at approximately 3 sccm. The unreacted CH_4/Ar flow is collected in a sealed chamber for products analysis. After the anaerobic oxidation process, Ar/water gas is purged for 1.5 h to remove any residual methane and wet the catalyst surface. The reactivation process continues for 1 hour. Upon the completion of reactivation process, the reactor is heated to 75℃ and an Ar flow is purged to collect the liquid for products analysis. Before starting the next cycle, the catalyst and the reactor are returned to the vacuum oven at 90 °C for 12 hours to remove any residual water.

The dual-states stepwise methane conversion using water microdroplets as oxidants was conducted in a homemade internal circulation methane oxidation apparatus, as shown in Fig. 1f, S1 and S2. The reaction system is sealed, and deionized water was atomized into ultrafine water microdroplets in atomization chamber, which are then pumped to the catalytic chamber by an internal circulation pump and sprayed onto the catalyst bed surface. A 300 W Xe lamp (full spectrum) was positioned above the catalyst bed to illuminate the catalyst surface through a quartz window. The resulting liquid water and products are collected directly in the bottom flask, while the products and water vapor in the gas phase are collected after passing through a condenser. Air in the apparatus is removed by 2 hours of argon purging, followed by an hour of methane purging to replace argon in the apparatus. Initially, the photocatalyst was pre-heated

under light irradiation for 15 minutes. Subsequently, the ultrasonic nebulizer was activated, and the resulting water microdroplets were transported onto the catalytic bed via an internal circulation pump.

S3. Microdroplet Experimental Apparatus

Apparatus overview. Methane oxidation with water microdroplets was performed in a closed gas-circulation loop (total internal volume ≈ 1.75 L) at ambient pressure. As shown in Figure S1, the setup comprises five modules arranged in series: (a) ultrasonic nebulization chamber → (b) reaction chamber → (c) condenser → (d) liquid collector → (e) circulation pump, and then back to (a) to complete the loop.

Ultrasonic nebulization chamber. The nebulizer chamber is a glass vessel with a conical top and cylindrical bottom (total height ≈ 18 cm; base diameter ≈ 6.5 cm). A commercial ultrasonic transducer (aluminum disc, diameter 5.0 cm; operating frequency 1.7 MHz; 24 V) is mounted at the bottom. The mist (i.e., water microdroplet) production rate in the ultrasonic nebulization chamber is regulated by a simple power–timing chain consisting of a CC/CV DC supply, a cyclic on/off timer, and a DC solid-state switch (MOSFET or SSR) connected in series with the nebulizer. The CC/CV module supplies a stable voltage and enforces a current limit to cap instantaneous/peak power and prevent over-drive. The cyclic timer sets independent ON and OFF durations (second-level resolution) and actuates the solid-state switch with no mechanical wear. The duty cycle $D=t_{on}/(t_{on}+t_{off})$ scales the time-averaged mist production rate ($mist_{avg} \approx D \times mist_{on}$). The mist delivered to the reaction chamber (i.e., the water deposition rate) is therefore tuned by two parameters—mist production rate and pump flow rate—providing a wide, stable, and reproducible operating range.

(b) Reaction chamber. Microdroplets entrained in the gas stream are delivered to a two-section glass reactor joined by a tapered neck that supports the catalyst bed. The upper section (height ≈ 7 cm; diameter ≈ 9 cm) is sealed with a quartz window to permit optical irradiation; the lower section (height ≈ 7.5 cm; diameter ≈ 4.5 cm) houses the outlet to the condenser.

(c) Condenser. Downstream gases and vapor pass through a water-cooled condenser (outer diameter ≈ 5 cm; length ≈ 25 cm). The condenser was cooled by a continuous circulation of cooling water (~5°C);

(d) Liquid collector. Condensate is routed to a cylindrical glass reservoir with a bottom inlet and top outlet to minimize re-entrainment of liquid into the circulating gas.

(e) Circulation pump. Loop circulation is driven by a miniature diaphragm pump with an adjustable flow rate (0-0.5 L/min). Unless otherwise specified, the loop was operated at ambient pressure.

Connection sequence. Nebulization chamber (a) → Reaction chamber (b) → Condenser (c) → Collector (d) → Circulation pump (e) → back to (a).

To quantify the water-droplet deposition rate under different operating conditions, the mist-laden flow was diverted to a $CaCl_2$ desiccant trap (with the condenser bypassed), and the mass increase over a fixed interval was measured gravimetrically and converted to liquid volume (ρ = 1.0 g mL^{-1}).

S4. Humidity-only Control (no microdroplets) Experiments.

We used the same homemade dual-state methane oxidation setup and only replaced the ultrasonic nebulizer with a PID-heated DI-water reservoir. The recirculating gas flowed over the water surface (through a splash guard/demister) to ensure no liquid carryover. Three reservoir temperatures were tested—T_w=30/45/60°C— yielding ≈40–55% RH, 70–80% RH, and >90% RH, respectively. For each T_w, we allowed 10–15 min to reach humidity steady state, then switched on the lamp and collected 1 h cumulative products.

S5. Reaction Orders Measurements.

Kinetic measurements were performed in the same sealed, internal-circulation apparatus and operating protocol used for standard tests (Fig. S1 and S2): Unless otherwise stated, total pressure was fixed at 1 atm, the light intensity were fixed at 10 suns. For the methane pressure-order (α) experiment, the microdroplet flux J_w was at 0.15ml/min; the methane partial pressure P_{CH4} was varied from 0.1 to 1.0 atm, with argon as the balance gas. Apparent order α was extracted from the slope of $\log_{10}$ rate vs. $\log_{10} P_{CH4}$ (linear regression). For the water-order (β) experiment, P_{CH4} were fixed at 0.7 atm; the microdroplet flux J_w was adjusted from 0.05-0.15ml/min. The apparent order with respect to droplets β was obtained from the slope of $\log_{10}$Rate vs. $\log_{10} J_w$.

S6. Apparent Activation Energy Measurements:

Powder catalyst was dispersed in deionized water and drop-cast onto a circular quartz disk (thickness 0.15 mm, disk diameter ≈3 cm). The slurry was confined to a 2 cm-diameter circular area at the center. The deposited catalyst mass was 200 mg, giving an areal loading of ~ 63.7 mg cm^{-2}. The coating was dried before use. We employed the same microdroplet-assisted methane-oxidation apparatus as in the routine experiments; the only modification was replacing the porous quartz-wool bed with a heated circular quartz disk. The disk rested on a resistive heater; a K-type thermocouple bonded to the disk backside enabled PID control. A 365–385 nm UV-A LED array illuminated the disk. The irradiance at the sample plane was set to ~85 mW cm^{-2}). With microdroplets as the sole oxidant, the reaction proceeds via rapid alternation between dry intervals and wet intervals. At a fixed droplet delivery rate, increasing the disk temperature shortens droplet residence and accelerates evaporation, increasing the time fraction spent effectively dry; decreasing temperature does the opposite. Therefore, by keeping the droplet feed fixed and only changing the disk temperature, we obtain temperature windows that are naturally "state-biased" without disrupting the required alternation. Wet-biased window: 65–85 °C (e.g., 65/70/75/80/85 °C), where slower evaporation sustains longer wet-contact intervals. Dry-biased window: 100–120 °C (e.g., 100/105/110/115/120 °C), where rapid evaporation limits wet contact and favors dry intervals. Water microdroplets feed was fixed at ~0.1 mL min^{-1}. Arrhenius plots of $\log_{10}$(rate) versus 1/T were constructed separately for the wet-biased and dry-biased windows to obtain $E_{a,\text{wet-biased}}$ and $E_{a,\text{dry-biased}}$.

S7. Product Analysis

The reaction products were analyzed using a combination of gas chromatography (GC–TCD/FID), gas chromatography–mass spectrometry (GC–MS), ^{1}H nuclear magnetic resonance (NMR), and colorimetric analysis. These complementary techniques enabled accurate identification and quantification of both gaseous and liquid products.

Gas-phase analysis. Gas products including CH_4, CO, CO_2, H_2, and C_2H_6 were analyzed using a gas chromatograph (Agilent 7890B) equipped with thermal conductivity (TCD) and flame ionization (FID) detectors. The TCD was employed for quantifying permanent gases (H_2, O_2, N_2, CO, and CO_2), while the FID was used for hydrocarbons (CH_4, C_2H_6). The system was

fitted with molecular sieve and porous polymer columns suitable for separating permanent gases and light hydrocarbons. Helium served as the carrier gas, and a fixed-volume gas loop of 2 mL ensured reproducible injections.

Liquid-phase analysis. Liquid products were first screened and identified by ^{1}H NMR spectroscopy (Bruker AVANCE III 400 MHz; D_2O as solvent). A small-molecule internal standard (maleic acid, typically 2 mM) was added to aid assignment. Characteristic resonances corresponding to methanol and formaldehyde were observed, while no higher oxygenates such as ethanol or acetic acid were detected above the detection limit. Quantitative determination of methanol was conducted using gas chromatography with flame ionization detection (GC–FID) under identical chromatographic conditions as those for gas analysis. The injection volume was 0.2 mL for all samples and standards, and each measurement was repeated at least three times to ensure reproducibility. Formaldehyde (HCHO) was quantified using the acetylacetone (Hantzsch/Nash) colorimetric method: samples were reacted with ammonium acetate, acetylacetone, and acetic acid at 60 °C for 10–30 min, and the absorbance was measured at 413 nm.

In isotope-labeling experiments using $^{13}CH_4$ or $H_2{}^{18}O$, GC–MS (Agilent 7890B coupled with 5977B MSD) was employed to confirm isotopic incorporation through mass shifts of methanol.

S8. Apparent Quantum Yield and Light-to-Chemical Energy Calculation

Monochromatic excitation was provided by narrow-band LEDs at 350, 355, 365, 385, 405, and 450 nm. A second lamp (xenon) equipped with long-pass filtering ($\lambda > 800$ nm) supplied thermal input only to reproduce droplet evaporation; its photons were not counted. We calculate the total apparent quantum yield (AQY) as follow equation:

$$\mathrm{AQY_{total}}(\%) = \frac{2n_{CH_3OH} + 4n_{HCHO} + 2n_{C_2H_6} + 6n_{CO} + 8n_{CO_2}}{N_{ph}} \times 100$$

where n_i is the amount of product i and N_{ph} is the number of incident photons.

The wavelength-resolved AQY values were used to calculate the light-to-chemical energy efficiency, $\eta_{LCEE}(\lambda)$. Because methanol is the dominant product, we evaluate energy storage using the net reaction:

$$CH_4 + H_2O \rightarrow CH_3OH + H_2$$

for which the standard Gibbs free-energy gain is $\Delta G_{net} \approx 115$ kJ mol^{-1}. Accordingly,

$$\eta_{LCEE}(\lambda) = AQY_{CH_3OH}(\lambda)\frac{\Delta G_{net}}{2h\nu}$$

where hν is the photon energy. The factor of 2 accounts for the two-electron process associated with CH_3OH formation

S9. Calculation of Methane-to-Methanol Selectivity and TOF

$$Selectivity\ of\ methanol = \frac{Rate_{CH_3OH}}{Rate_{CH_3OH} + Rate_{HCHO} + Rate_{CH_3CH_3} + Rate_{CO} + Rate_{CO_2}}$$

$$Selectivity\ of\ ethane = \frac{Rate_{CH_3CH_3}}{Rate_{CH_3OH} + Rate_{HCHO} + Rate_{CH_3CH_3} + Rate_{CO} + Rate_{CO_2}}$$

$$TOF = \frac{Yield}{molar\ amount\ of\ catalyst}$$

To simplify the calculations, we assume that for all catalysts, the number of active sites account for 10% of the total catalyst mass. The calculated values can only be used as a basis for comparing TOFs of different reaction modes and cannot be used for comparison with other references.

S10. Characterization of the Catalyst

The STEM image was conducted using a JEOL 3100R05 double-corrected S/TEM operated at 300 kV. The X-ray photoelectron spectroscopies were collected using a Kratos Axis Ultra XPS with a monochromatic Al source. The binding energy of Ga 3*d* was used for the internal calibration. The room temperature photoluminescence spectroscopy measurements were conducted using a 325 nm He-Cd laser as the excitation source. The X-ray diffraction profile data were collected on Rigaku Miniflex 600. The Cu Kα line was utilized for the irradiation.

S11. In Situ DRIFTS Measurements

In situ DRIFTS spectra were conducted using a Bruker infrared spectrometer equipped with a liquid nitrogen-cooled mercury-cadmium-telluride detector. The experiments were conducted under anaerobic conditions, and the apparatus is evacuated and purged with argon for two hours to remove any air present. The catalyst-loaded quartz-disk is initially pretreated in the Harrick

reactor at 100 °C for 30 minutes under an argon atmosphere. After cooling to room temperature, a gas mixture of methane and argon (CH_4/Ar = 1:5) is first introduced into the Harrick reactor at a flow rate of 5 sccm for 1 h. Subsequently, the catalyst was irradiated with light for 30 mins, after which the flow was switched to H_2O/Ar for another 20 mins.

S12. Computational Methods

Free energy calculations were performed using the plane wave DFT based Vienna Ab initio Simulation Package (VASP.5).(1-3) Using a cutoff energy of 450 eV, the core electrons were described via projected-augmented wave potentials.(4, 5) The PBE functional(6) with D3 dispersion corrections (including Becke-Johnson damping)(7, 8) was chosen as exchange correlation functional, using Gaussian type smearing with a σ value of 0.1 eV. A Monkhorst-Pack type(9) grid of 3x3x1 kpoints was used to sample the Brillouin-zone. DFT+U was used to adjust the d-band energies of the Zn, with a U_{eff} = 2.50 eV.(10) Optimizations were performed until the convergence criteria of 0.02 eV/Å for the forces of and $1x10^{-6}$ eV per unit cell for energies for reached. Optimizations were followed by frequency analysis, with only displacements of the adsorbates considered keeping computational cost in mind, using the finite difference method with a step size of 0.015 Bohr. Using the vaspkit1.3 postprocessing program,(11) free energy corrections were estimated within the harmonic approximation with these obtained frequencies. Here, a temperature of 298 K and a pressure of 1 atm was employed. The computational hydrogen electrode model of Nørskov et al. was applied to estimate free energies of proton and electron.(12) To model the ZnO, a bulk optimization was applied on a supercell of 16 atoms, including optimization of the crystal vectors. The resulting geometry was then rotated such that the polar O terminated surface (0001) normal was aligned with the z axis, with the Zn terminated at the lower end. The box was then expanded, resulting in a box size of a=6.402 Å, b=10.316 Å, c=30.000 Å to ensure a vacuum layer between O and Zn terminated surface planes. Dipole corrections along z were applied. The simulation box, including a total 4 double layers (one Zn and one O layer each), of which the top and bottom double layer were allowed to relax, while the inner double layers were frozen in bulk geometry, is visualized using the VESTA program in Fig. S20. The nonpolar $(10\bar{1}0)$ surface was constructed similarly, resulting in a box of a=6.402 Å, b=10.316 Å, c=30.000 Å shown in Fig.

241 S21. Energies, free energy corrections and free energies for all reactants, products and
242 intermediates are given in tables S2-S4.
243

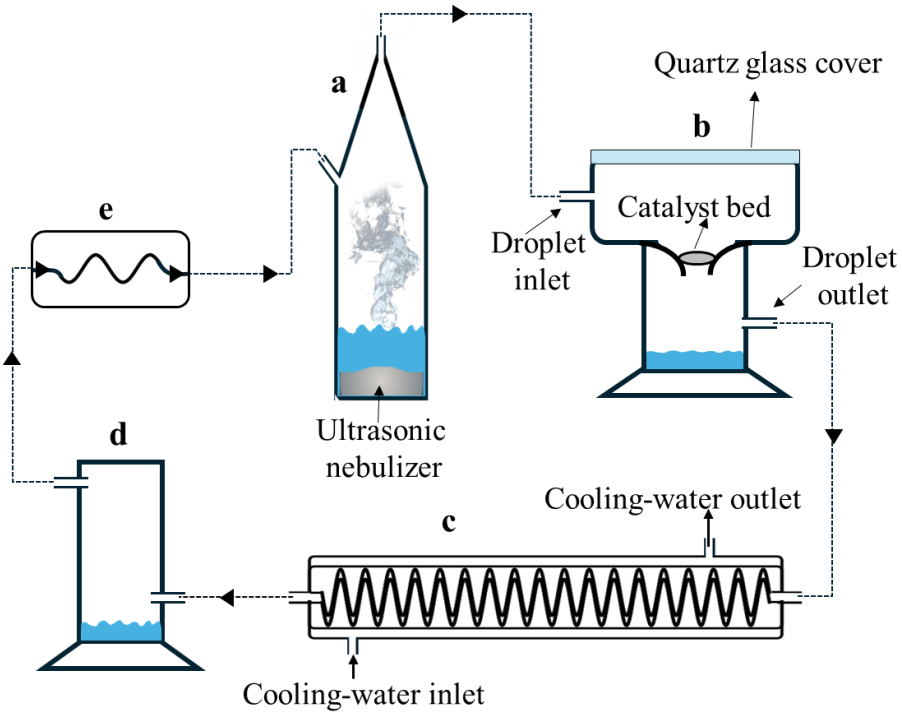

Fig. S1 Schematic illustration of the self-designed water-droplet methane oxidation reactor system. The system consists of (a) an ultrasonic nebulization chamber, (b) a reaction chamber with a catalyst bed covered by a quartz window, (c) a condenser equipped with circulating cooling water, (d) a condensate collector, and (e) a diaphragm circulation pump. The arrows indicate the gas flow direction in the closed circulation loop.

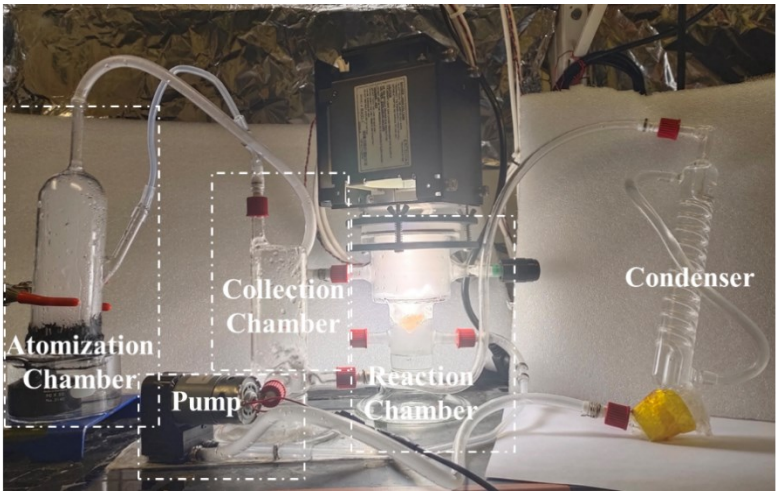

Fig. S2 The digital image of the apparatus used for photocatalytic methane oxidation with water microdroplets as the sole oxidant.

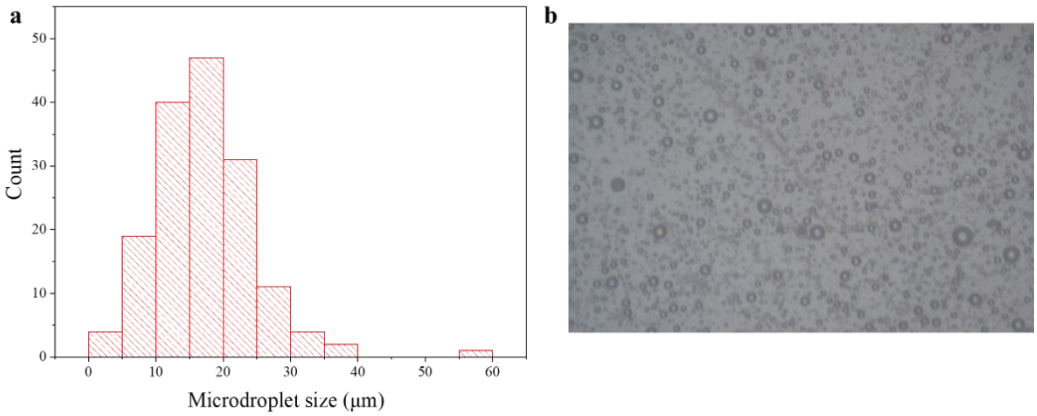

Fig. S3. (a) Size distributions of water microdroplets generated by the ultrasonic nebulizer with (b) representative optical micrographs.

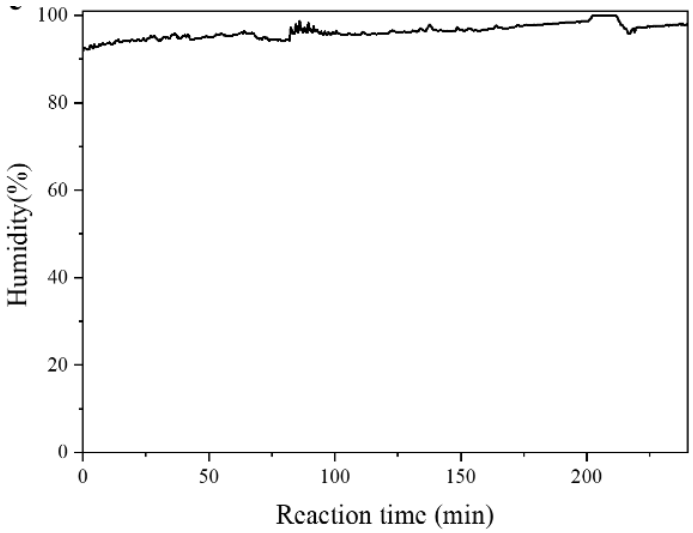

Fig. S4. Time evolution of the relative humidity inside the droplet-assisted methane oxidation reaction chamber during operation.

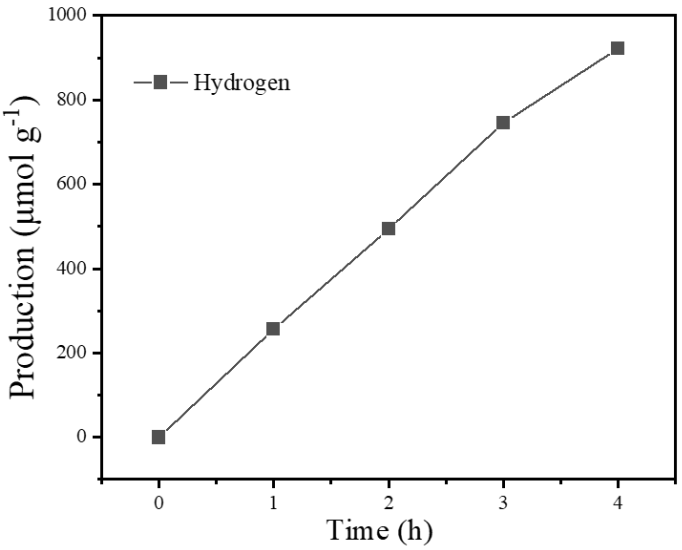

Fig. S5 The production of hydrogen in dual-states stepwise methane oxidation using water microdroplet as the oxidant.

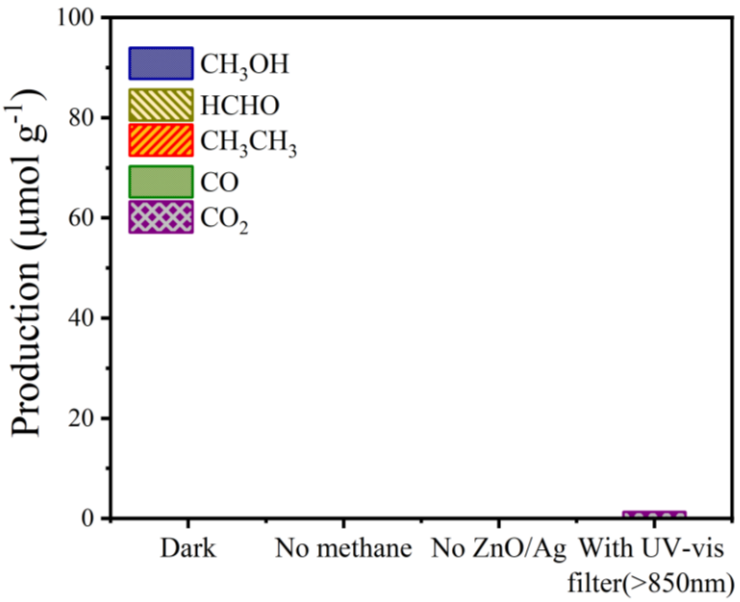

Fig. S6 The experimental results on dual-states stepwise methane oxidation using water microdroplets as the oxidant under various conditions.

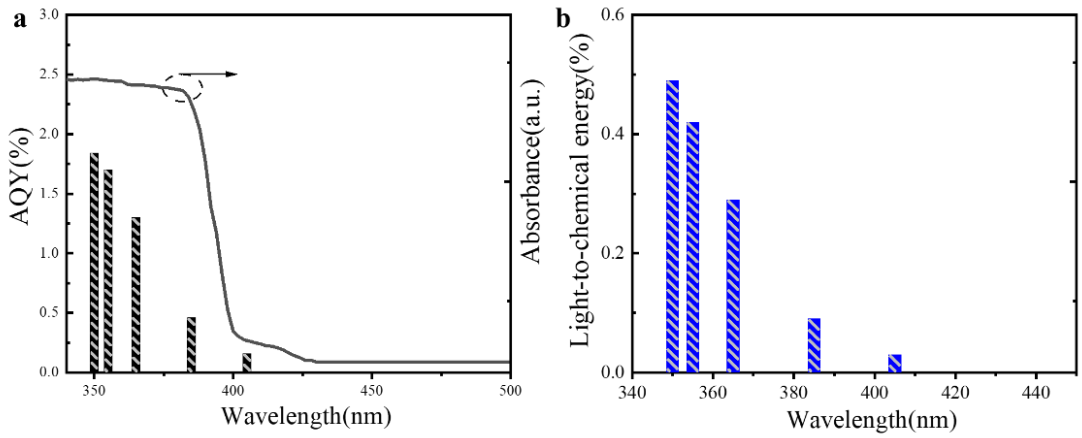

Fig. S7. (a) Apparent quantum yield (AQY) of ZnO/Ag measured under monochromatic excitation (350–450 nm). (b) Corresponding light-to-chemical energy conversion efficiency, obtained from the AQY data by converting photon flux to chemical enthalpy.

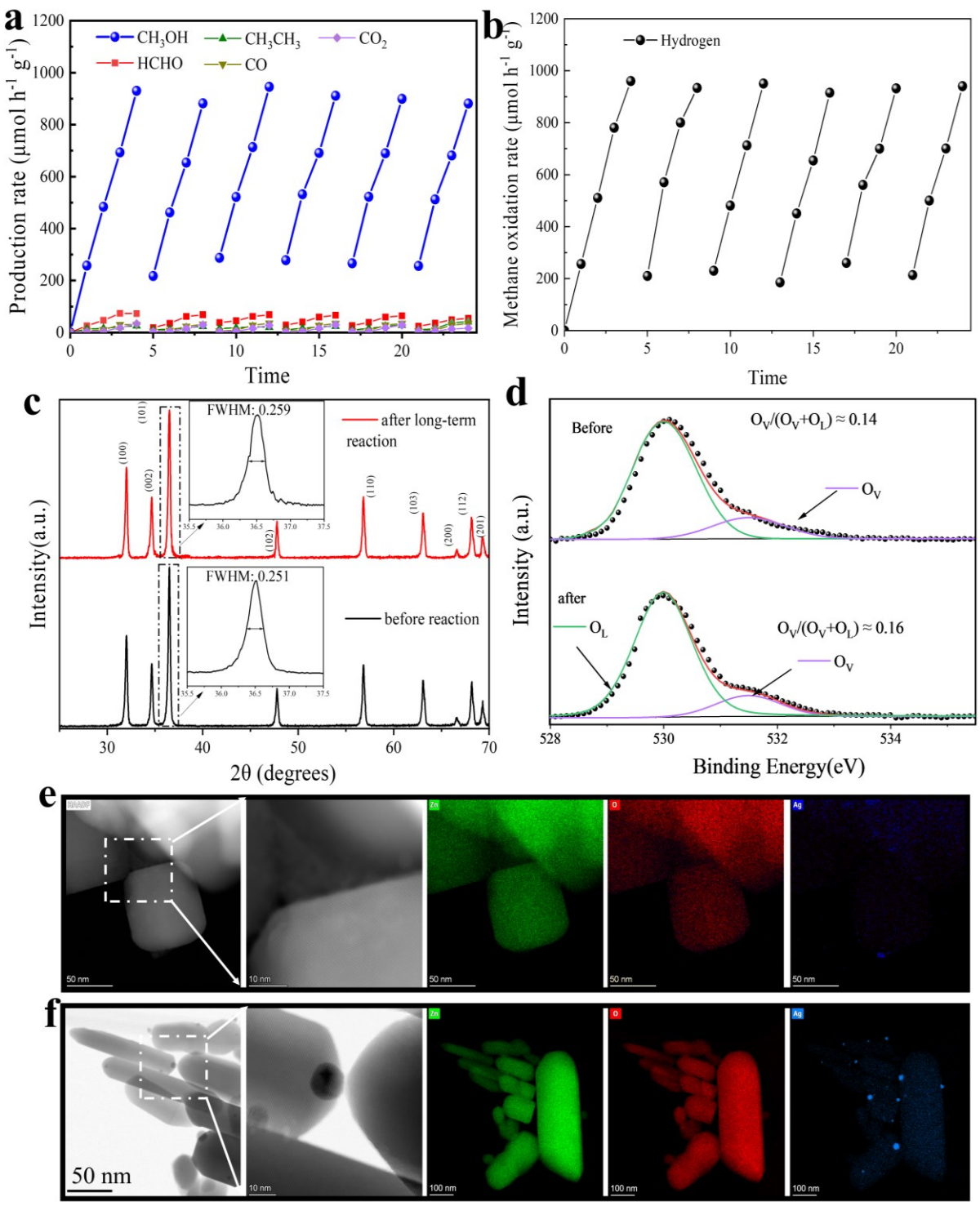

Fig. S8 Performance and structural stability of ZnO/Ag during water microdroplet-assisted methane oxidation. (a, b) Product distributions over six consecutive 4 h cycles (total 24 h) under water microdroplet-enabled CH_4 oxidation on ZnO/Ag. (c) XRD patterns of fresh vs. 24 h–spent catalysts, showing no detectable change in crystallinity. (d) XPS O 1s deconvolution for fresh vs. 24 h–spent samples, indicating no increase in the surface oxygen-vacancy

component. (e, f) TEM images before and after reaction, revealing no discernible morphology or dispersion changes after 24 h operation.

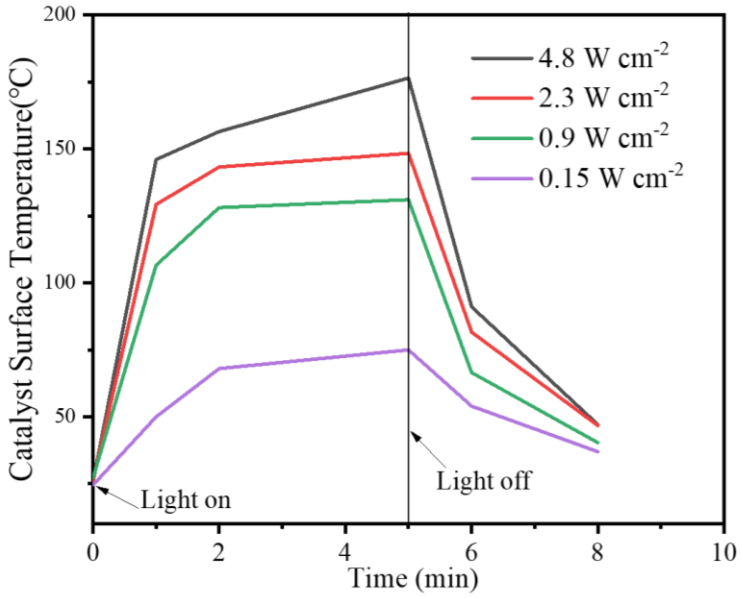

Fig. S9 The surface temperature changes of the catalyst-loaded reaction bed over time under illumination with different intensities.

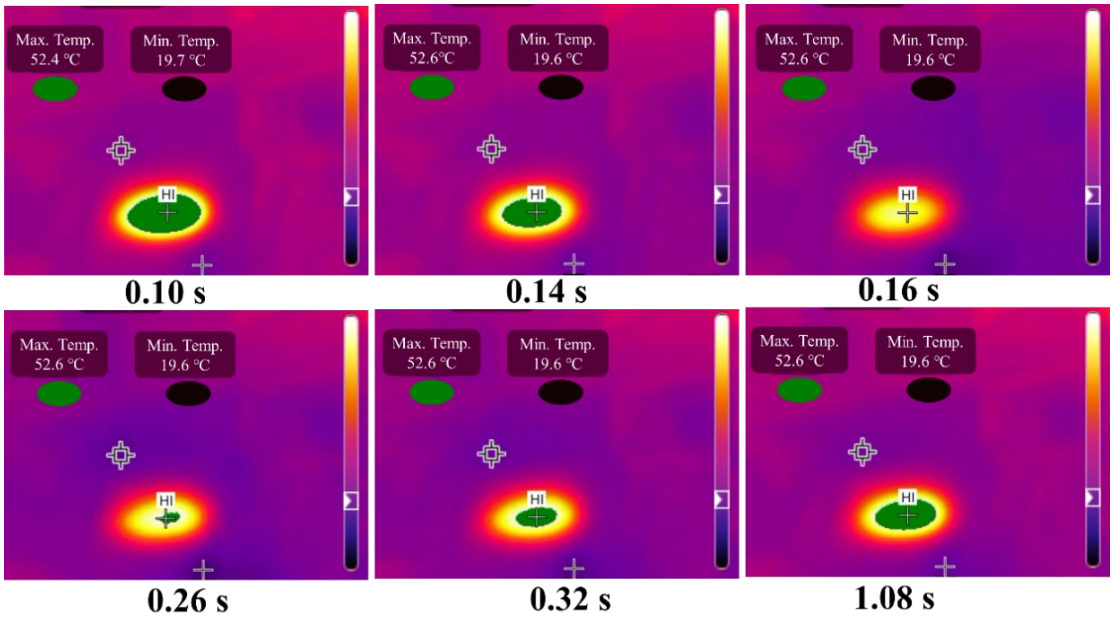

Fig. S10 Infrared camera characterization of rapid microdroplet evaporation on the reaction bed surface. The change of the catalyst surface from a wet state to a dry state was observed by monitoring the catalyst surface temperature. A microdroplet was sprayed onto the catalyst surface at 0.14 s, the illumination intensity is 0.1 W cm^{-2}. Limited by the camera frame rate, surface temperature changes with higher light intensity are difficult to capture.

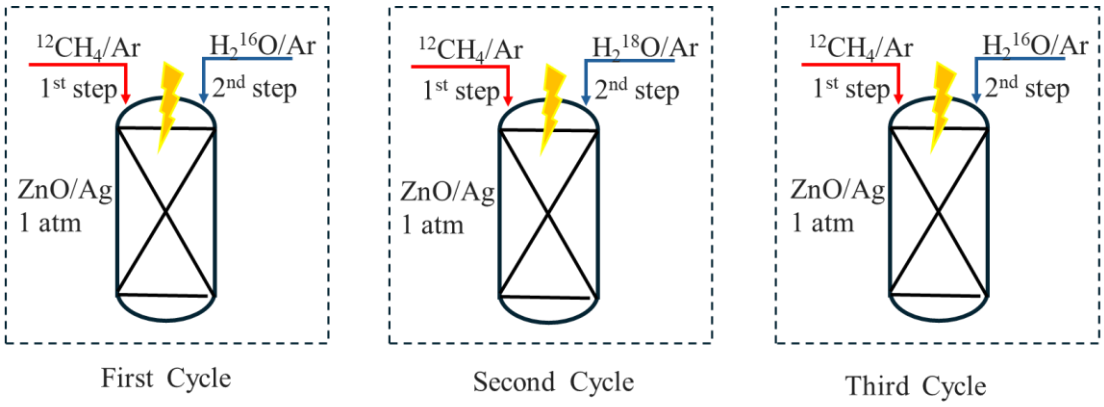

Fig. S11 A schematic illustration of the conventional stepwise methane oxidation process, highlighting the dynamic transitions between the dry (methane-rich, 1st step) and wetting (water-rich, 2nd step) states of the catalyst surface. $H_2{}^{18}O$ isotope labeling in the second cycle is used to track the oxygen source.

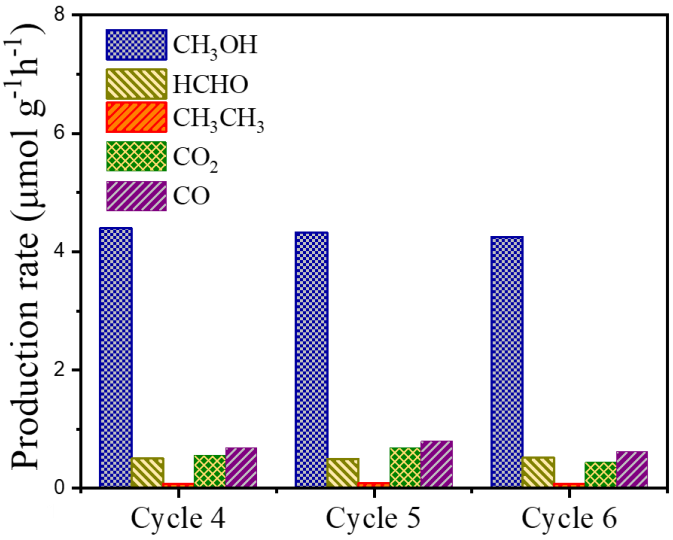

Fig. S12 Methane oxidation products during methane anaerobic oxidation process in cycles 4-6 of conventional stepwise methane oxidation.

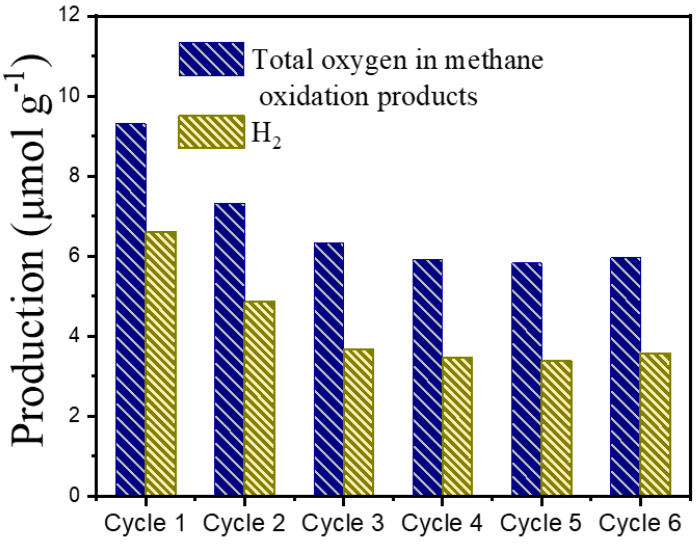

Fig. S13 Total oxygen in all methane oxidation products produced during methane anaerobic oxidation process and the hydrogen gas generated during the water reduction process in each cycle of conventional stepwise methane oxidation.

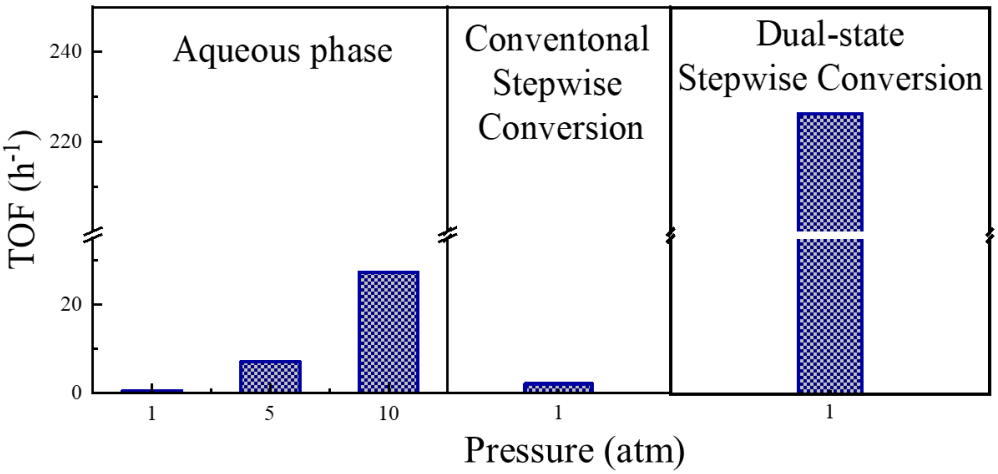

Fig. S14 Comparison of catalytic TOF under different methane oxidation reaction conditions. To streamline the calculations, it is assumed that surface active sites constitute 10% of the total catalyst mass for ZnO/Ag samples.

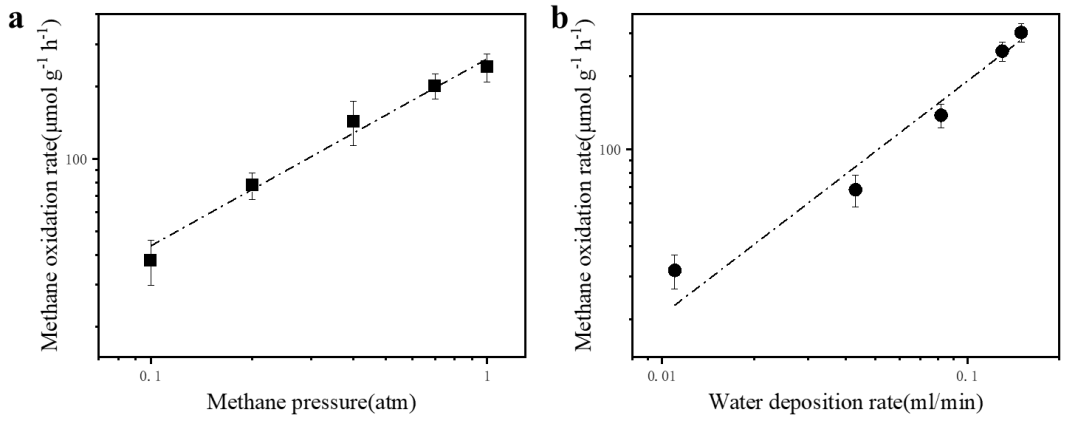

Fig. S15 Kinetic signatures and state-biased activation energies for water microdroplet-assisted methane oxidation. (a) $Log_{10}(CH_4$ oxidation rate) vs. $Log_{10}(P_{CH4})$ under CH_4/Ar (balance Ar), total pressure is 1 atm; microdroplet feed J_w=0.15 mL min^{-1}; Xe lamp, ~12 suns. The slope gives the reaction order with respect to methane (α). **(b)** $Log_{10}(CH_4$ oxidation rate) vs. $Log_{10}(J_w)$ under pure CH_4, 1 atm; Xe lamp, ~12 suns; 0.05 ml $min^{-1} < J_w \leq 0.15$ ml min^{-1}. The slope gives the reaction order with respect to microdroplet deposition rate (β).

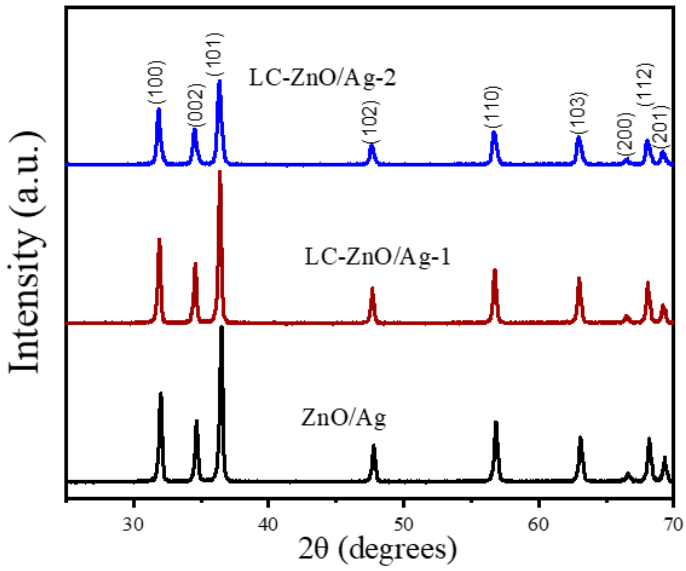

Fig. S16 X-ray diffraction (XRD) spectra of ZnO/Ag, LC-ZnO/Ag-1 and LC-ZnO/Ag-2 samples.

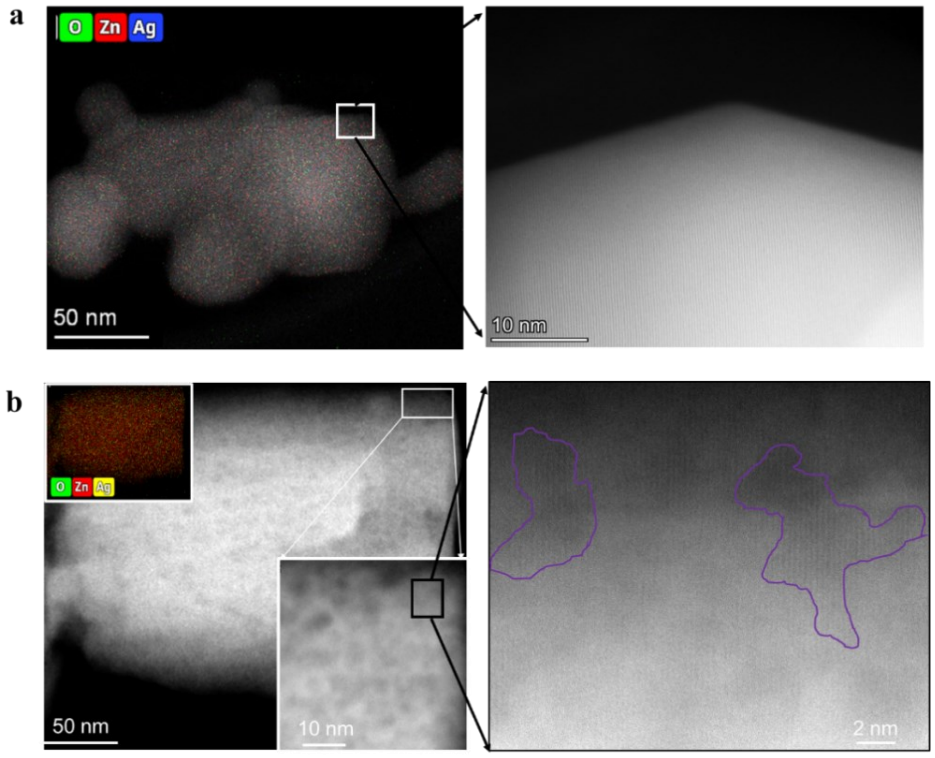

Fig. S17 The high-angle annular dark-field (HAADF) scanning transmission electron microscopy (STEM) images of (a) ZnO/Ag and (b) LC-ZnO/Ag-1

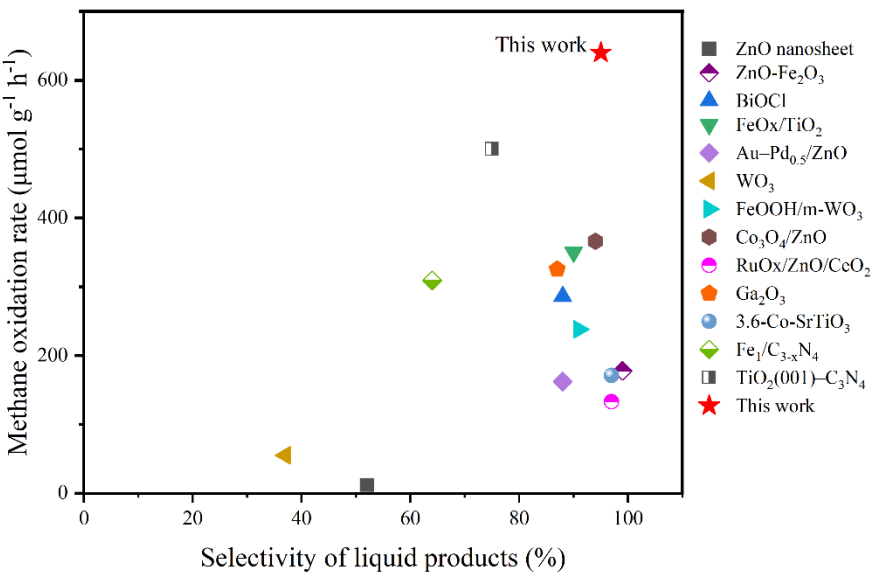

Fig. S18 Performance comparison of this work with representative photocatalytic methane oxidation studies conducted at 1 atm. Marker types/colors correspond to different catalyst/oxidant systems as indicated in the legend; detailed sources is listed in Table S1.

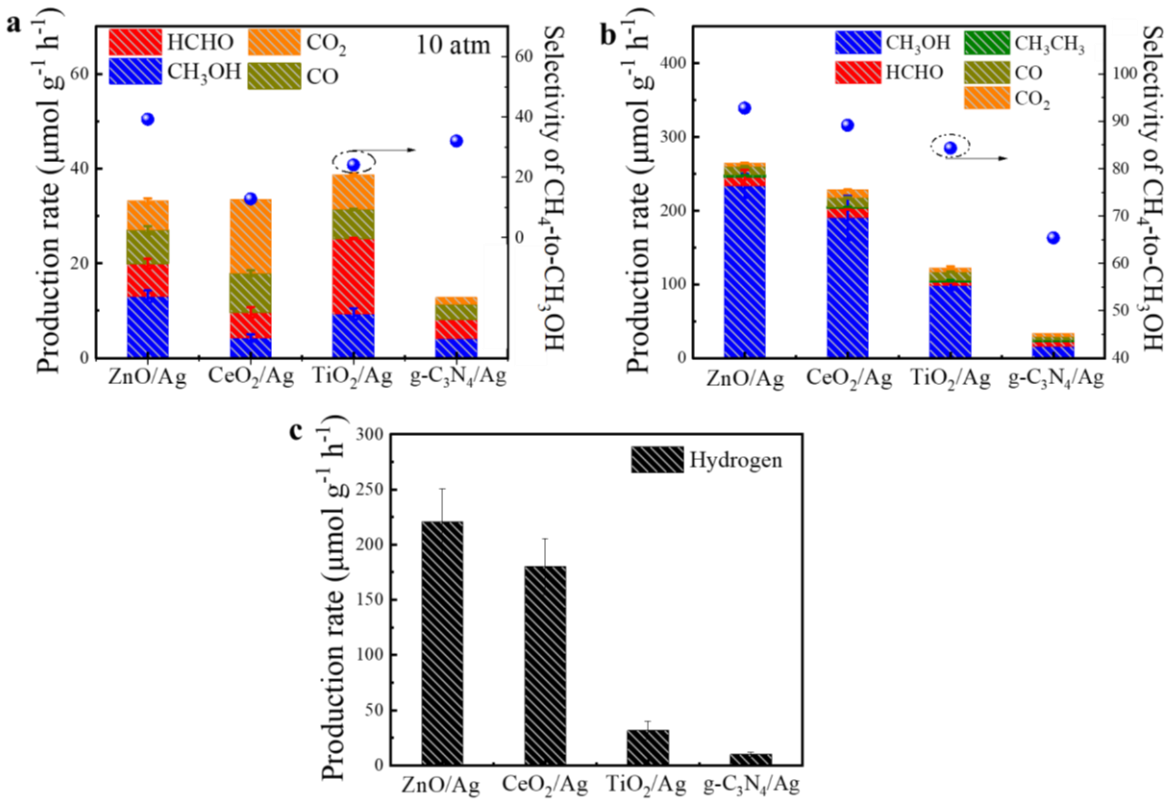

Fig. S19 Product rates and selectivity for methane oxidation with different photocatalyst. (a) High-pressure aqueous-phase methane oxidation. (b, c) Microdroplet-assisted methane oxidation. In all panels, blue dots denote the selectivity from CH_4 to methanol, while the stacked bars show the formation rates of individual products.

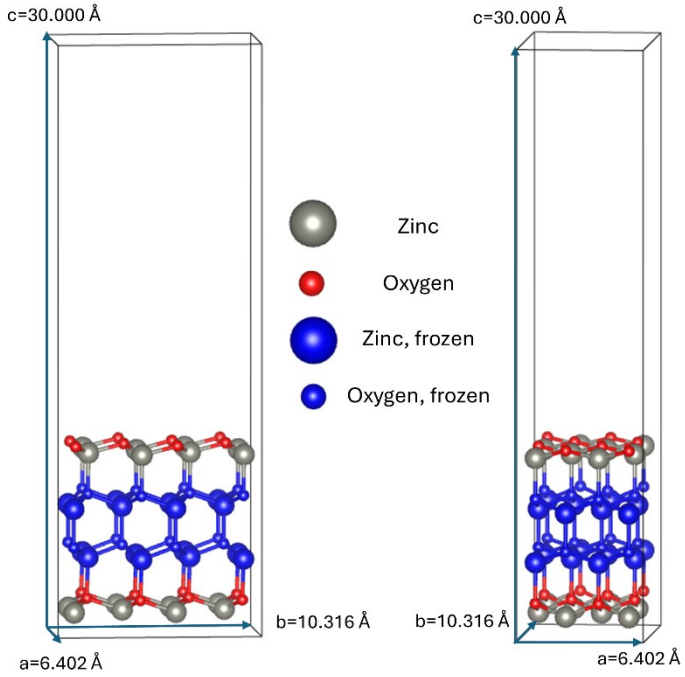

Fig. S20. Simulation box of the polar O-terminated surface of ZnO with view along the a-axis (left) and the b-axis (right). Frozen atoms are shown in blue.

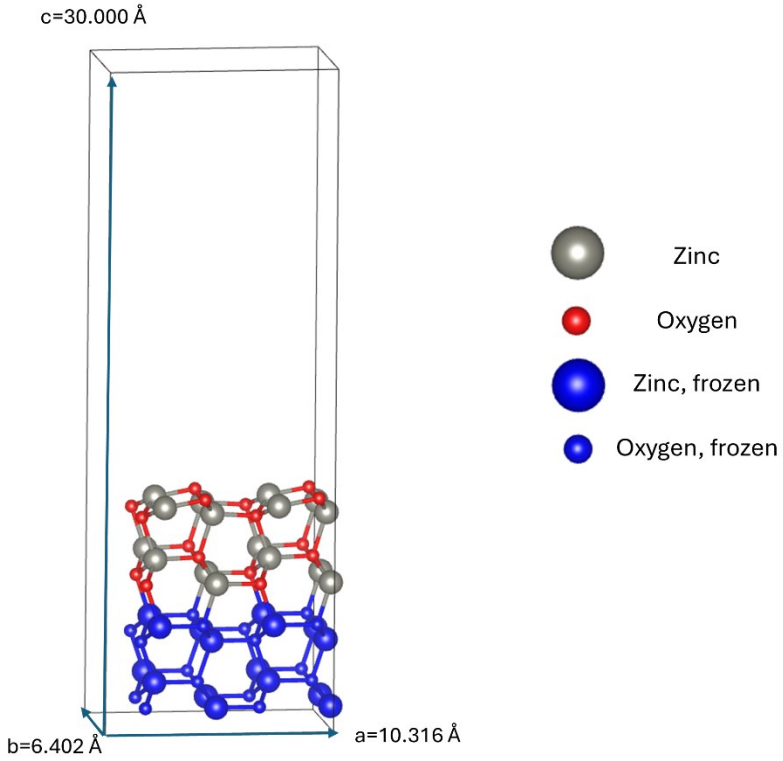

Fig. S21. Simulation box of the non-polar O-terminated surface of ZnO with view along the a-axis (left) and the b-axis (right). Frozen atoms are shown in blue.

Fig. S22. Geometries and free energies of reaction for the reaction steps on non-polar ZnO surface.

Table S1 Representative high-performance studies of photocatalytic methane-to-oxygenates at ambient pressure (1 atm).

Catalysts	Oxidant	Production rate /μmol g^{-1} h^{-1}	Selectivity of liquid products	Reference
ZnO nanosheet	H_2O	~12	~52%	(13)
ZnO-Fe_2O_3	H_2O	~178	~99%	(13)
BiOCl	H_2O	~286	~88%	(14)
FeO_x/TiO_2	O_2/H_2O	~350	~90%	(15)
Au–$Pd_{0.5}$/ZnO	H_2O_2	~162	~88%	(16)
WO_3	O_2/H_2O	~55	~37%	(17)
FeOOH/m-WO_3	H_2O_2	~238	~91%	(18)
Co_3O_4/ZnO	H_2O_2	~366	~94%	(19)
RuO_x/ZnO/CeO_2	H_2O	~133	~97%	(20)
Ga_2O_3	O_2/H_2O	~325.4	~87%	(21)
TiO_2(P25)	O_2/H_2O	~265.3	~25%	(21)
ZnO	O_2/H_2O	~212.3	~38%	(21)
Fe1/$C_{3-x}N_4$	O_2/H_2O	~171	~97%	(22)
3.6-Co-$SrTiO_3$	H_2O	~309	~64%	(23)
TiO_2(001)–C_3N_4	O_2/H_2O	~510	~75%	(24)
ZnO/Ag	O_2/H_2O	~640	~95%	This work

Table S2. Electronic energies, Gibbs free energy corrections and Gibbs free energies of gas phase molecules.

Molecule	**Electronic energy [eV]**	**Free energy correction term [eV]**	**Gibbs free energy [eV]**
Hydrogen (H_2)	-6.77	-0.05	-6.82
H_2O	-14.25	+0.09	-14.16
Methane (CH_4)	-24.07	+0.72	-23.35
Methanol (CH_3OH)	-30.27	+0.74	-29.53

Table S3. Electronic energies, Gibbs free energy corrections and Gibbs free energy of all intermediates on ZnO(0001). All atoms considered in the frequency calculations for free energy corrections are marked in green.

Intermediate	Electronic energy [eV]	Free energy correction term [eV]	Gibbs free energy [eV]
ZnO	-274.54	0.00	-274.54
ZnO_v	-268.61	0.00	-268.61
ZnO*H	-280.18	+0.31	-279.87
ZnO*H	-280.18	+0.38	-279.80
ZnO*CH_3	-296.58	+1.00	-295.58
ZnO*CH_3	-296.58	+1.07	-295.51
ZnO*CH_3_ZnO*H	-301.76	+1.31	-300.46
ZnO*CH_3_ZnO*H	-301.76	+1.38	-300.38

Table S4. Electronic energies, Gibbs free energy corrections and Gibbs free energy of all intermediates on ZnO($10\bar{1}0$). All atoms considered in the frequency calculations for free energy corrections are marked in green

Intermediate	Electronic energy [eV]	Free energy correction term [eV]	Gibbs free energy [eV]
ZnO	-285.85	0.00	-285.85
Zn*CH_3_O*H	-310.07	+1.15	-308.89
O*CH_3_O*H	-308.35	+1.23	-307.08

References

1. G. Kresse, J. Hafner, Ab Initio Molecular Dynamics for Liquid Metals. *Phys. Rev. B* **47**, 558-561 (1993).
2. G. Kresse, J. Furthmüller, Efficiency of Ab-Initio Total Energy Calculations for Metals and Semiconductors using a Plane-wave Basis Set. *Comput. Mater. Sci.* **6**, 15-50 (1996).
3. G. Kresse, J. Furthmüller, Efficient Iterative Schemes for Ab Initio Total-Energy Calculations using a Plane-Wave Basis Set. *Phys. Rev. B* **54**, 11169 (1996).
4. G. Kresse, D. Joubert, From Ultrasoft Pseudopotentials to the Projector Augmented-Wave Method. *Phys. Rev. B* **59**, 1758 (1999).
5. G. Kresse, J. Hafner, Norm-Conserving and Ultrasoft Pseudopotentials for First-Row and Transition Elements. *J. Phys.-Condens. Mat.* **6**, 8245 (1994).
6. J. P. Perdew, K. Burke, M. Ernzerhof, Generalized Gradient Approximation Made Simple. *Phys. Rev. Lett.* **77**, 3865 (1996).
7. S. Grimme, S. Ehrlich, L. Goerigk, Effect of the Damping Function in Dispersion Corrected Density Functional Theory. *J. comput. chem.* **32**, 1456-1465 (2011).
8. S. Grimme, J. Antony, S. Ehrlich, H. Krieg, A Consistent and Accurate Ab Initio Parametrization of Density Functional Dispersion Correction (DFT-D) for the 94 Elements H-Pu. *J. Chem. Phys.* **132** (2010).
9. H. J. Monkhorst, J. D. Pack, Special Points for Brillouin-Zone Integrations. *Phys. Rev. B* **13**, 5188 (1976).
10. S. Ding *et al.*, Oxygen-vacancy-type Mars-van Krevelen mechanism drives ultrafast dioxygen electroreduction to hydrogen peroxide. *Mater Today Energy* **38** (2023).
11. V. Wang, N. Xu, J.-C. Liu, G. Tang, W.-T. Geng, VASPKIT: A User-Friendly Interface Facilitating High-throughput Computing and Analysis using VASP Code. *Comput. Phys. Commun.* **267**, 108033 (2021).
12. J. K. Nørskov *et al.*, Origin of the Overpotential for Oxygen Reduction at a Fuel-Cell Cathode. *J. Phys. Chem. B* **108**, 17886-17892 (2004).
13. K. Zheng *et al.*, Room-Temperature Photooxidation of CH_4 to CH_3OH with Nearly 100% Selectivity over Hetero-ZnO/Fe_2O_3 Porous Nanosheets. *J. Am. Chem. Soc.* **144**, 12357-12366 (2022).
14. Y. Chen *et al.*, Dual-Function Reaction Center for Simultaneous Activation of CH_4 and O_2 via Oxygen Vacancies during Direct Selective Oxidation of CH_4 into CH_3OH. *ACS Appl. Mater. Interfaces* **13**, 46694-46702 (2021).
15. J. Xie *et al.*, Highly Selective Oxidation of Methane to Methanol at Ambient Conditions by Titanium Dioxide-Supported Iron Species. *Nat. Catal.* **1**, 889-896 (2018).
16. Q. Zhou *et al.*, Selective Photocatalytic Oxidation of Methane to Methanol by Constructing a Rapid O_2 Conversion Pathway over Au–Pd/ZnO. *ACS Catal.* **14**, 955-964 (2024).
17. K. Villa, S. Murcia-López, T. Andreu, J. R. Morante, Mesoporous WO_3 Photocatalyst for the Partial Oxidation of Methane to Methanol using Electron scavengers. *App. Catal. B: Environ.* **163**, 150-155 (2015).
18. J. Yang, J. Hao, J. Wei, J. Dai, Y. Li, Visible-Light-Driven Selective Oxidation of Methane to Methanol on Amorphous FeOOH Coupled m-WO_3. *Fuel* **266**, 117104 (2020).

19. Z. Xiao *et al.*, Intermediate Stabilization for Tuning Photocatalytic Selective Oxidation of CH_4 to CH_3OH over Co_3O_4/ZnO. *J. Catal.* **413**, 20-30 (2022).
20. D. Yu *et al.*, Solar Photocatalytic Oxidation of Methane to Methanol with Water over RuOx/ZnO/CeO_2 Nanorods. *ACS Sustainable Chem. Eng.* **10**, 16-22 (2021).
21. C. Han *et al.*, Selective Cleavage of Chemical Bonds in Targeted INtermediates for Highly Selective Photooxidation of Methane to Methanol. *J. Am. Chem. Soc.* **145**, 8609-8620 (2023).
22. Z. Zhang *et al.*, Photo-Splitting of Water toward Hydrogen Production and Active Oxygen Species for Methane Activation to Methanol on Co-$SrTiO_3$. *Chem Cataly.* **2**, 1440-1449 (2022).
23. L. Li *et al.*, Modulation of Single-Iron-Atom Coordination Environment Toward Three-Electron Oxygen Reduction for Photocatalytic CH_4 Conversion to CH_3OH. *Small* **21**, 2500835 (2025).
24. X. Sun *et al.*, Molecular Oxygen Enhances H_2O_2 Utilization for the Photocatalytic Conversion of Methane to Liquid-Phase Oxygenates. *Nat. Commun.* **13**, 6677 (2022).